Available online at www.sciencedirect.com
SCIENCE DIRECT®
Journal of Power Sources 144 (2005) 54–66
JOURNAL OF POWER SOURCES
www.elsevier.com/locate/jpowsour

Flow distribution in a bipolar plate of a proton exchange membrane fuel cell: experiments and numerical simulation studies

F. Barreras*, A. Lozano, L. Valiño, C. Marín, A. Pascau

LITEC/CSIC María de Luna 10, 50018 Zaragoza, Spain

Received 5 August 2004; received in revised form 24 November 2004; accepted 29 November 2004
Available online 26 February 2005

Abstract

An experimental and numerical research has been performed in order to study the flow distribution in a bipolar plate of a commercial PEM fuel cell. Planar laser induced fluorescence (PLIF) trace tracking has been applied to visualize the flow pattern and to measure the velocity in the plate channels. Simultaneously, the problem has been studied numerically, simulating the flow under similar operational conditions as those fixed in the experiments. Results obtained reveal a defective design of the bipolar plate. Based on the experimental visualization and on the numerical simulations it is concluded that the flow preferentially moves through the lateral channels, resulting in an inappropriate distribution on the electrode surfaces. Velocity measurements also confirm the above statements, showing high values at the lateral channels, while the flow is nearly stagnant in the central region. With this non-homogeneous flow distribution at the bipolar plate, a low performance of the fuel cell energy conversion could be expected.

Keywords: PEM fuel cells; Bipolar plate; Fluid mechanics; Flow field; Visualization; Modeling

1. Introduction

The energy demand worldwide is growing at an alarming rate. This demand is responded by an increase in the combustion of fossil fuels, with the entailed problems of pollutant emissions, greenhouse effect and acid rain. Besides, the natural reserves of fossil fuels are diminishing and a substantial increase in their price can be expected in the foreseeable future. In view of this situation, hopes have been deposited in fuel cells as a key solution for the 21st century energy problems, enabling clean and efficient production of heat and power from a diversity of primary sources [1].

Fuel cells are devices that generate electricity by a chemical reaction. Despite the general belief that they represent a new technology, their basic working principles have been known for centuries. Strictly speaking, they were first demonstrated in 1843 with the experiments of Sir William R. Grove. Fuel cells have two electrodes, anode (negative) and cathode (positive), where the reaction that produces electricity takes place. Between them, there is an electrolyte, which allows the transport of electrically charged particles from one electrode to the other, and a catalyst, which enables and speeds up the reaction. Depending on the electrolyte, fuel cells are usually divided into five different types, namely: alkali, molten carbonate, phosphoric acid, proton exchange membrane (PEM) and solid oxides. In general, hydrogen is normally used as the basic fuel, which reacts electrochemically with oxygen producing electricity and heat and, as a byproduct, water.

Proton exchange membrane fuel cells work with a polymeric electrolyte formed into a thin, very light and permeable sheet, at low temperature (around 80 °C). To speed up the chemical reaction, a platinum catalyst is used in both sides of the membrane. Electrons are removed from the hydrogen atoms in the anode and the resulting protons diffuse through the permeable membrane, migrating towards the cathode. The electrons pass from the anode to the cathode through an external circuit and provide electric power. At the cathode,

* Corresponding author. Tel.: +34 976 716 440; fax: +34 976 716 456.
E-mail address: felix@litec.csic.es (F. Barreras).

0378-7753/$ – see front matter © 2005 Elsevier B.V. All rights reserved.
doi:10.1016/j.jpowsour.2004.11.066

Nomenclature

d	inlet duct diameter (m)
E	error in the numerical simulation
n	iteration number in the numerical study
Q	volumetric flow rate (ml min^{-1} or l min^{-1})
Re	Reynolds number
v	velocity of the flow (m s^{-1} or cm s^{-1})
V	volume (m^3)
X	fraction of liquids in the mixture (%)

Greek symbols

β	criteria of convergence in the numerical simulation
ϕ	solution of the problem in the numerical study
μ	absolute viscosity (Pa s)
ρ	density (kg m^{-3})
ν	kinematics viscosity (m^2 s^{-1})

Subscripts and superscripts

glyc.	glycerin
H_2	hydrogen
liq.	liquids
mixt.	mixture
wat.	water

electrons, protons and oxygen combine to form water. PEM fuel cells have been widely used since the early days of the space programs, as well as in submarine vessels. The strict environmental regulations on air quality have also motivated the introduction of this technology in the automotive industry. In the same way, PEM fuel cells have also been used in stationary power applications. Today, the broad spectrum of applications for PEM fuel cells includes their use in portable devices such as cellular telephones or laptop computers.

The efficiency in energy conversion achieved in PEM fuel cells is higher than that in power plants or internal combustion engines. This efficiency can be reached as the result of a set of complex physical and chemical processes occurring simultaneously, which are strongly dependent on the fuel and oxygen fluid dynamics inside the fuel cell. It is easy to understand that optimization of PEM fuel cells performance requires a deep comprehension of the current density behavior as a function of the operational conditions. In this sense, several studies have been performed applying numerical techniques [2–4]. From the experimental viewpoint, some methods used have been aimed to study the water production and its influence on the mass transport inside the fuel cell [5–9].

A singular component of PEM fuel cells is the bipolar plate, as the first stage of the flow distribution system. In general, the functions of this element are to guide the flow of reactant gases, and, in the case of fuel cell stacks, to provide electron conduction paths from one cell to another. So, in order to ensure a correct operation of the fuel cell it is necessary both a suitable material and the proper topology to optimize the gas flow distribution. Common materials used in bipolar plates are graphite, some metals (stainless steel, titanium, etc.), or composite materials [10], which should be lightweight, and easy to manufacture. They must also be impermeable to gases, and have high electrical and thermal conductivities. A low performance of the fuel cell energy conversion, as well as a waste of the very expensive platinum catalyst could be expected if the flow distribution in the bipolar plate is non-homogeneous.

There are different plate structures that produce different flow fields as, for example, squared spot, interdigitated, serpentine, spirals, cascade and series–parallel, with geometries of various complexity levels. Alternatively, flow through porous carbon or perforated stainless steel plates have also been used. A comparative analysis of the advantages and disadvantages of some of the above topologies can be found in the reviews by Carrette et al. [11] or Costamagna and Srinivasan [12]. Hontañón et al. [13] studied the gas flow distribution system of a PEM fuel cell using 3D numerical simulations. Their results indicated that porous materials yielded better flow distributions compared to grooved plates in terms of reactant gas utilization. Recently, Dohle et al. [14] studied the interaction between the diffusion layer and the flow field exiting a meander channel bipolar plate in a direct methanol fuel cell. Based also on numerical simulations, they concluded that even a meander structure distributes the reactants non-homogeneously on the electrodes.

In this study, an experimental and numerical research has been performed in order to study the flow distribution in a commercial parallel channel bipolar plate. To this end, flow visualization using laser-induced fluorescence, as well as measurements of the velocity field by dye trace tracking have been applied. On the other hand, a 2D numerical simulation of the flow distribution based on the Navier–Stokes equations has also been performed. Results obtained from both experimental and numerical studies have been compared. Both of them reveal a non-homogeneous flow distribution across the bipolar plate, which will, probably produce a limited performance of the fuel cell energy conversion. The excellent agreement between the experimental results and the numerical predictions confirms the validity of the numerical code to study design variations without the need of actually fabricating the plates.

2. The problem under study

The experiments have been performed using a commercial bipolar plate with a rough surface area of 50 cm^2. It is formed by 16 central channels 1 mm deep and 3 mm wide, separated by ribs with a 1 mm thickness. Two channels in the upper and lower part of the plate and two lateral channels, all of them with a width of 2 mm, surround the whole flow area.

The internal diameter of both inlet and outlet ducts is 2 mm. This type of bipolar plates is normally used to distribute the oxygen (or air) and hydrogen over the cathode and anode, respectively. However, this study has been focused on the visualization of the hydrogen flow pattern distribution. In this case, a single fuel cell with a volumetric flow of $1\,l\,min^{-1}$ ($1.67 \times 10^{-5}\,m^3\,s^{-1}$) at 80 °C has been considered [15]. Under this flow condition, the single fuel cell should produce a power close to 50 W, corresponding to a current density of $400\,mA\,cm^{-2}$ and a voltage of 2.5 V.

Gas flow visualization has been widely used in fluid mechanics but its application involves some complexities difficult to circumvent in some experimental setups. For example, ultraviolet laser radiation is needed to induce the fluorescence of the typical vapor tracers used to visualize the flows, such as acetone or acetaldehyde. In this case, a quartz window is needed to seal the bipolar plate in the front-face where the images are to be recorded. Additionally, these organic vapors cannot be used in conjunction with many plastic materials that are quickly degraded. For these reasons, a dimensional analysis has been performed to replace the gas by a liquid, ensuring the dynamic similarity between the real problem and the model. The main physical properties of hydrogen at 80 °C considered in the analysis [16,17] are: absolute viscosity (μ) of 1.05×10^{-5} Pa s and density (ρ) equal to $0.0674\,kg\,m^{-3}$, resulting in a kinematic viscosity (ν) of $1.558 \times 10^{-4}\,m^2\,s^{-1}$.

A gas entrance velocity of $5.3\,m\,s^{-1}$ results from a simple calculation for the hydrogen flow (v_{H_2}) using the volumetric flow rate considered and the area of the inlet duct. The resulting Reynolds number ($Re = v_{H_2} d/\nu$) based on the inlet duct diameter (d) is 68. In order to perform the experiments under dynamic similarity when a liquid is used, new operational conditions have to be considered to maintain the Reynolds number unchanged, as this dimensionless group is the one that essentially determines the flow characteristics. Two conditions are imposed to the selected liquid: it has to be transparent, and the fluorescent dye that will be used has to be easily soluble in it. For simplicity, only three candidates have been considered, water, glycerin and methanol. The main physical properties for the three fluids at 20 °C [16] are shown in Table 1. If flow dynamic similarity is imposed to the selected liquid, Eq. (1) is used to calculate the liquid velocity, as well as the volumetric flow rate

$$Re_{mod} = 68 = \frac{v_{liq.} d}{\nu_{liq.}} \tag{1}$$

Results obtained applying Eq. (1) to the three selected liquids are displayed in Table 2. It is evident that extremely low flow velocities have to be managed if water or methanol is used in the experiments. Under these experimental conditions the liquid flow will be largely perturbed by the dye injection. On the other hand, a quite high velocity flow has to be supplied if glycerin is used, due to its high viscosity value. In this case, a huge pressure is needed to overcome the pressure drop inside the bipolar plate, making the watertight seal of the model a difficult task.

To solve all of these problems a mixture of glycerin and water has been selected. For example, if a volumetric flow rate of $230\,ml\,min^{-1}$ is fixed, which corresponds to a velocity of $1.22\,m\,s^{-1}$, a mixture kinematic viscosity value of 24.1 cSt ($24.1 \times 10^{-6}\,m^2\,s^{-1}$) is needed. The mixture composition can be calculated using the methodology described in [16] for aqueous systems applying the following set of equations:

$$\nu_{mixt.} = \frac{\mu_{wat.}^{X_{wat.}} \mu_{glyc.}^{X_{glyc.}}}{\rho_{mixt.}} \tag{2}$$

$$\rho_{mixt.} = X_{wat.}\rho_{wat.} + X_{glyc.}\rho_{glyc.} \tag{3}$$

where X represents the volumetric fraction of both liquids defined by

$$X_{liq.} = \frac{V_{liq.}}{V_{mixt.}} \tag{4}$$

Solving the equations, a kinematic viscosity of $24.1 \times 10^{-6}\,m^2\,s^{-1}$ requires a mixture composition of 49.6% of glycerin and 51.4% of water.

3. Experimental facilities

Having in mind the above-calculated values for the experimental conditions, the experimental facility displayed in Fig. 1 has been used in the experiments. It includes the bipolar

Table 1
Physical properties of the liquids considered in the study at 20 °C

	Hydrogen	Water	Glycerin	Methanol
Density, ρ ($kg\,m^{-3}$)	0.0674	998	1.236	788.5
Absolute viscosity, μ (Pa s)	1.05×10^{-5}	1.003×10^{-3}	0.7601	5.99×10^{-4}
Kinematic viscosity, ν ($m^2\,s^{-1}$)	1.558×10^{-4}	1.005×10^{-6}	6.15×10^{-4}	7.6×10^{-7}

Table 2
Velocity and volumetric flow rate calculation for the three liquid fluids considered

	Hydrogen	Water	Glycerin	Methanol
Velocity, v	$5.3\,m\,s^{-1}$	$3.42\,cm\,s^{-1}$	$20.91\,m\,s^{-1}$	$2.58\,cm\,s^{-1}$
Volumetric flow rate, Q	$1.0\,l\,min^{-1}$	$6.45\,ml\,min^{-1}$	$3.94\,l\,min^{-1}$	$4.86\,ml\,min^{-1}$

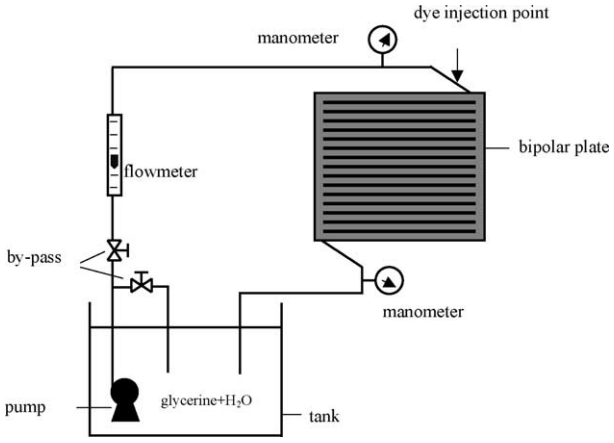

Fig. 1. Experimental setup.

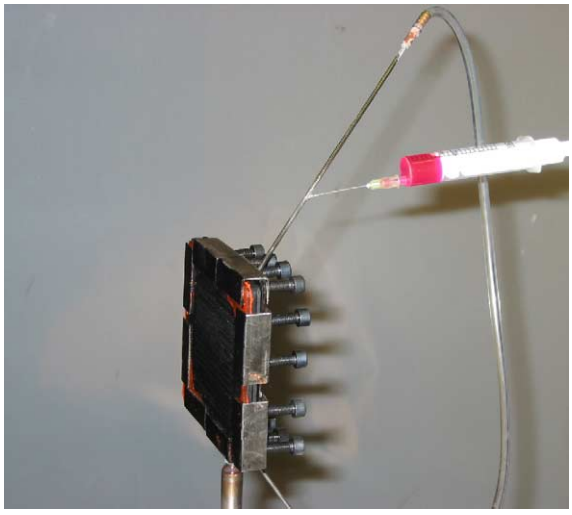

Fig. 2. Detail of the dye injection system.

plate, a 10 l tank, an immersion pump capable of supplying a maximum flow rate of 100 l min^{-1}, two manometers and a flowmeter with a maximum reading of 1.7 l min^{-1}. A by-pass has been included before the bipolar plate assembly to avoid large pressure drops and, hence, liquid overheating. This is very important due to the exponential dependence of the liquid mixture viscosity on temperature, which might cause large fluctuations on the flow conditions. The dye injection point is placed 80 mm (40 diameters) upstream of the inlet point, and consists of a 1 mm capillary welded at an angle of 45° with respect to the axis of the inlet duct. A photograph of the injection system can be seen in Fig. 2. This figure also shows the transparent plastic cover that seals the bipolar plate and constitutes the front-face of the experimental model. It is to be noted that the inlet and outlet ports are tilted with respect to the plate edges.

Two different flow rates have been tested, 230 and 350 ml min^{-1}. Before acquiring the images, the liquid was allowed to circulate during 5 min to stabilize the flow in stationary conditions. After this time, dye was injected in pulses, in synchronization with the laser pulses and the image acquisition.

To visualize the flow pattern, laser induced fluorescence (LIF) has been applied, using Sulforhodamine B (Kiton Red) dissolved in the water/glycerin mixture as the luminescent tracer. To excite the dye, a double cavity Quantel YG781C-10 pulsed Nd:YAG laser has been used, doubling the frequency of its emission to obtain 100 mJ pulses at 532 nm, with a pulse duration of 6 ns. The absorption spectrum of Sulforhodamine B has a maximum at 556 nm; hence excitation at 532 nm is very efficient [18]. The fluorescence peak of this dye is located at 620 nm, which allows for an efficient discrimination between the emitted signal and the excitation laser light beam. To further decrease the background light, a Schott OG 550 filter has been placed in front of the camera lens, blocking any residual 532 nm wavelength from the incident laser beam.

To image the fluorescence emission, a Princeton Instruments slow scan CCD camera has been used, with a 50 mm *f*#1.2 Nikon lens, placed perpendicular to the bipolar plate. As depicted in Fig. 3, a spherical lens with a focal distance of −25 mm has been placed at 1 m of the bipolar plate to expand the laser beam obtaining a slightly divergent cylinder of light, which illuminates the plate at an angle of 60° with respect to the axis of the camera. This arrangement does not introduce any perspective distortion in the images and eliminates any possible direct reflection of the laser light on the CCD camera. Data sets have been recorded for a field of view of 70 mm × 94 mm with a spatial resolution of 245 μm pixel^{-1}.

Velocity field in the channels has been measured by tracking the evolution of the dyed liquid using the same optical

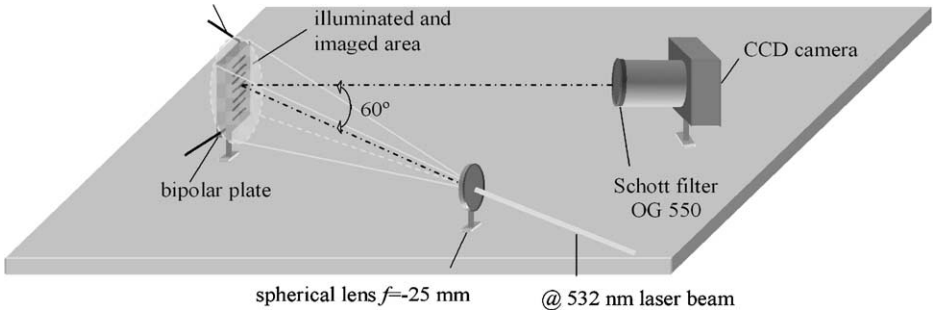

Fig. 3. Optical setup for visualization and PIV experiments.

arrangement and laser source previously described for the visualization experiments. An interlined Hamamatsu ORCA-ER CCD camera with a resolution of 1024 × 1024 pixels has been employed to record the image sequences. The time interval between successive images was set to 0.5 s and the correlation between them has been analyzed to track the displacement of the dyed liquid front.

4. Numerical simulation

In order to numerically study the present configuration, a computer code has been adapted to simulate the flow described in the previous section. As numerical simulations are relatively cheap, this code will be a tool to study possible alternative geometrical configurations in the future.

A first approach to simulate this flow is to consider a 2D geometry. In principle this seems a rather limiting simplification, given the non-homogeneous nature of the flow in the coordinate removed. However, the most important issue that influences the flow pattern is the pressure distribution near the entrance. This pressure distribution can be adequately reproduced with a 2D simulation, so the flow rate in each channel of the plate will match reasonably well the experimental results, as it will be seen later. Other assumptions, such as isothermal, incompressible and laminar flow, and a steady final solution, have been included to match the experimental conditions.

The resulting transport equations governing the flow in the channels of the bipolar plate are the steady version of the well known Navier–Stokes equations for mass and momentum conservation:

$$\nabla(\rho\vec{v}) = 0 \tag{5}$$

$$\nabla(\rho\vec{v}\cdot\vec{v}) = -\nabla p + \nabla(\mu\nabla\vec{v}) + \rho\vec{g} \tag{6}$$

A finite volume method [19] has been preferred over finite elements to discretize the coupled Eqs. (5) and (6), given the simple geometrical configuration of the channels in the bipolar plate. Finite differences have not been considered due to the non-conservative character of this discretization method.

To improve the velocity–pressure coupling a (regular Cartesian) staggered grid, that is, shifted half a cell in x and y directions for calculating x and y components of the velocity field, has been used. This coupling is numerically implemented using a SIMPLE [20] algorithm. Finally, a gradient–conjugate technique has been used to iteratively solve the resulting linear equation system.

To accommodate the 2D numerical simulation to the 3D physical problem is essential to preserve the Reynolds number in the channel. For a real flow rate, this imposes a 2D flow rate given through the following relationship:

$$Q_{3D} = \frac{\pi}{4} d Q_{2D}. \tag{7}$$

So, for a volumetric flow of 230 ml min^{-1} and a Reynolds number of 68, the corresponding 2D inlet velocity is 1.22 m s^{-1}, which equals that obtained from the experimental analysis.

In the real configuration, the inlet duct forms an angle with the XY plane, which is not reproducible in a 2D approximation. As a result, the eddy that appears near the entrance might be shifted with respect to the experimental position. This eddy can be influential in the general flow pattern in the channel, for this reason, it is very important to reproduce its actual position as accurately as possible. This has been done by introducing the fluid at 5 mm from the corner of the plate, and by properly choosing the incidence angle (70° respect to the horizontal axis). However, it has been verified that the actual position of the eddy is not too sensitive to this two parameters.

Although the flow is steady, the numerical scheme requires an initial condition to begin the simulation. A constant (in modulus) small velocity has been considered through all the channels. The numerical value has been chosen to preserve mass conservation.

5. Error analysis

To study the effect of the discretization on the numerical solution, different grid sizes (69 × 69, 138 × 138, 207 × 207) have been considered. The calculation of the velocity field of the flow for these three grids is depicted in Fig. 4. As can be seen, the flow behavior obtained is quite similar even when the flow is simulated using relatively coarse grids. It can also be observed that meshes 138 × 138 and 207 × 207 show very similar results, which indicates that the intermediate mesh has a spatial resolution high enough to simulate with a good precision the flow conditions in the bipolar plate. The results of the 69 × 69 mesh converged after 50,000 iterations with a level of convergence β less than 10^{-6}, being even lower for the other two grids. This coefficient β is defined in the following way: assuming that the solution after each iteration behaves as a Cauchy series, an error can be defined associated to each iteration as

$$\begin{aligned} E_0 = |\phi_1 - \phi_0| \geq E_1 = |\phi_2 - \phi_1| \geq \cdots \geq E_n \\ = |\phi_{n+1} - \phi_n| \geq \cdots 0. \end{aligned} \tag{8}$$

Extending the previous idea to define an error associated between two levels of iteration, using the triangle inequality,

$$\begin{aligned} |\phi_{n_2} - \phi_{n_1}| \leq |\phi_{n_2} - \phi_{n_2-1}| + \cdots + |\phi_{n_1} - \phi_{n_1-1}| \\ \leq |n_2 - n_1||\phi_2 - \phi_1|, \end{aligned} \tag{9}$$

it is obtained

$$E_{n_2-n_1} \equiv \frac{|\phi_{n_2} - \phi_{n_1}|}{|n_2 - n_1||\phi_2 - \phi_1|}. \tag{10}$$

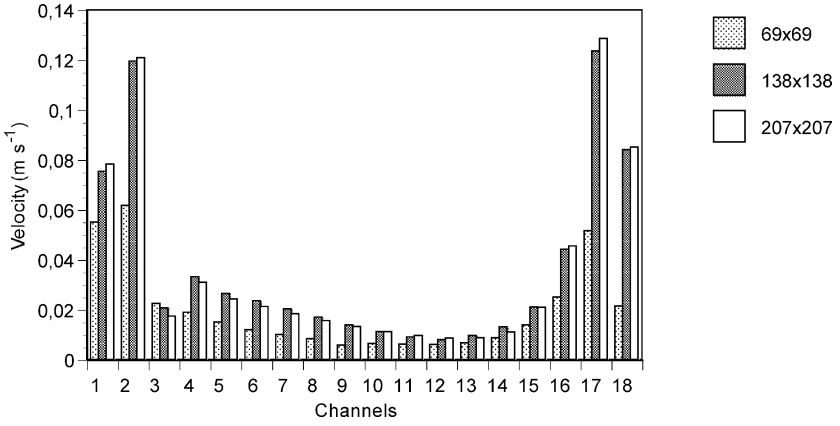

Fig. 4. Calculation of velocity values of the flow in the different channels for the three grids.

This is a non-dimensional error with values between 0 and 1. A criteria or level of convergence β is reached when

$$E_{n_2-n_1} \leq \beta; \quad \forall x \tag{11}$$

The influence of the number of iterations in the convergence of the solution has also been analyzed. Results are presented in Fig. 5 for the intermediate grid (138×138), which shows that the velocity in the penultimate channel takes longer to converge. A physical explanation to this issue is that the flow in this channel is mainly affected for the presence of the outlet duct, which is very close, causing a slower setting of a proper pressure field at its exit. To minimize errors due to this influence, the first 5 mm of the exit pipe have been included in the simulation domain. A detailed description of the convergence error for this grid size is depicted in Fig. 6,

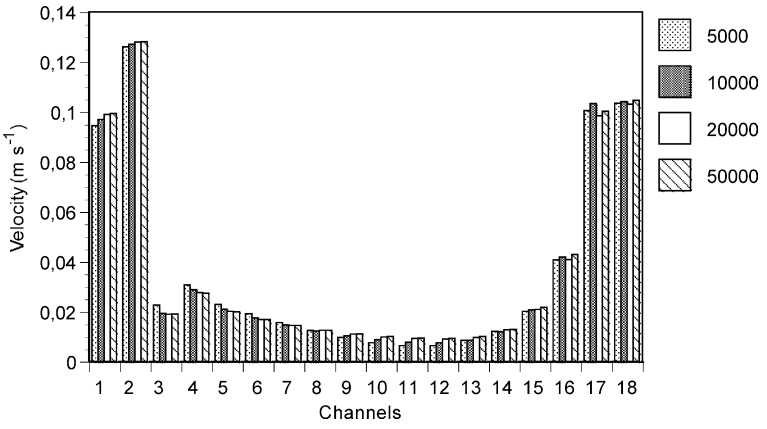

Fig. 5. Influence of the number of iterations in the convergence of the solution of the numerical study.

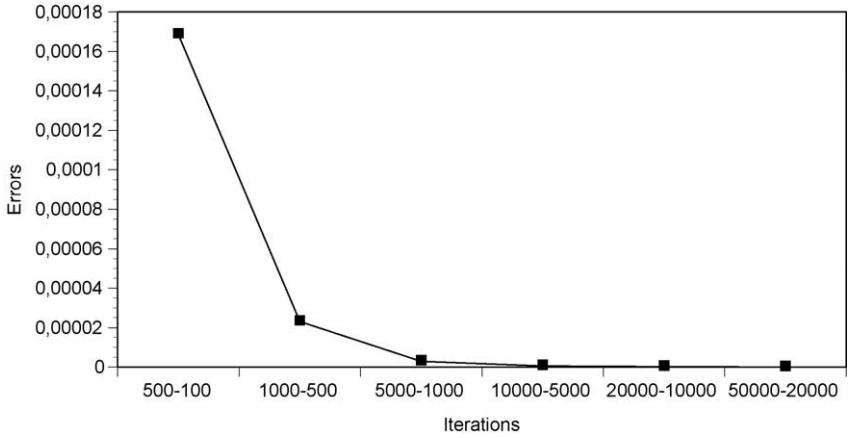

Fig. 6. Influence of the convergence error for the 138×138 grid as a function of the number of iteration steps.

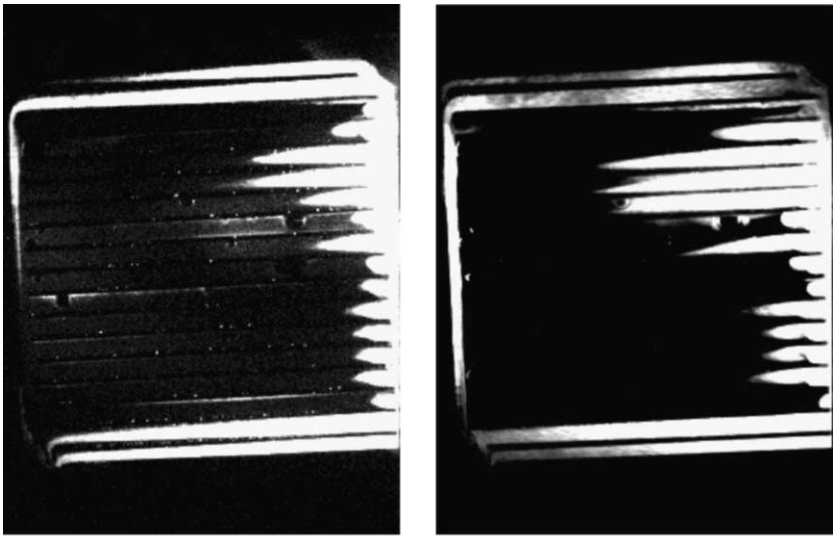

(a) (b)

Fig. 7. Visualization images obtained for two different water flows: (a) 230 ml min^{-1} and (b) 350 ml min^{-1}.

which shows the error $E_{n_2-n_1}$ in the channel cross section averaged velocities for six different number of iterations. It certainly shows a good numerical behavior.

6. Results

As a first step of the experimental research, some preliminary tests were performed using water. The aim of these experiments was to check the overall efficiency of the experimental set up. In this case, a thorough control of the temperature variation of the fluid at the reservoir to evaluate the efficiency of the by-pass system, as well as the control of the seeding method was performed. In Fig. 7, a sample of the acquired images can be observed for two different volumetric flow rates, 230 and 350 ml min^{-1}, which correspond to Reynolds numbers of 2.120 and 3.714, respectively. It should be noted that in all the images, the fluid inlet is located in the upper right corner, and liquid flows from right to left.

Once the experimental system had been tested, experiments with the glycerin–water mixture were performed. The kinematic viscosity of the final mixture was experimentally measured with a Rheotest viscosimeter, adjusting in situ the desired value by slightly varying the fraction of liquids in the mixture. An example of the recorded images is displayed in Fig. 8 for the same volumetric flow rates as in Fig. 7, 230 and 350 ml min^{-1}, corresponding to Reynolds numbers of 68 and 154. One striking feature of Figs. 7 and 8 is the similar-

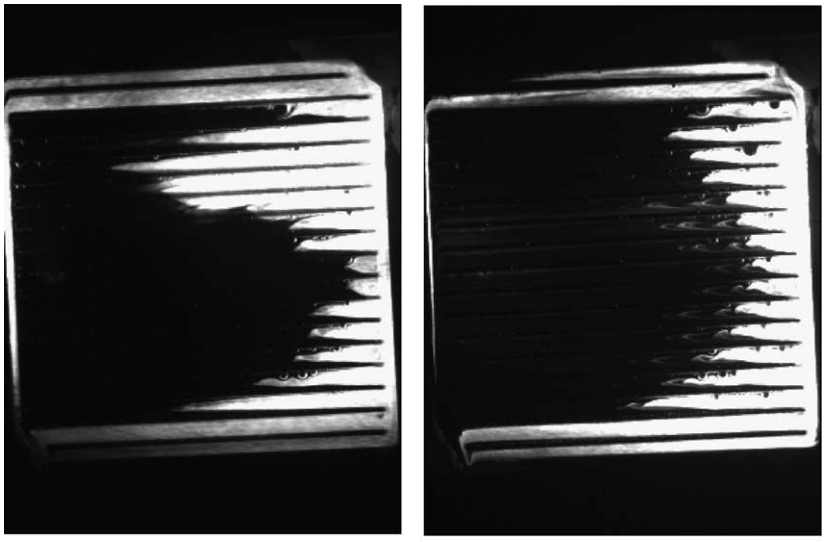

(a) (b)

Fig. 8. Visualization images for two different glycerin + water flows: (a) 230 ml min^{-1} and (b) 350 ml min^{-1}.

ity of the dye pattern for water and the mixture inside the bipolar plate. The large difference in Reynolds number for both flows indicates that the flow distribution is independent either of the flow conditions or the fluid physical properties and suggests very low turbulence levels. Flow visualization results show a very poor efficiency of the bipolar plate tested regarding to flow distribution. The presence in the images of channels practically depleted of any dye trace is indicative of absence of flow circulation, in contrast to the preferred circulation along the lateral channels. The flow of dyed fluid through the lateral (upper and lower) channels, as well as the higher dilution of dye concentration in these areas clearly indicates a substantially higher velocity compared to that of the central zone of the bipolar plate where the dye concentration is homogeneously distributed.

Fig. 9 presents a sequence of the temporal evolution of the dye front progressing across the plate. The temporal interval between successive images is 0.5 s. Some details have

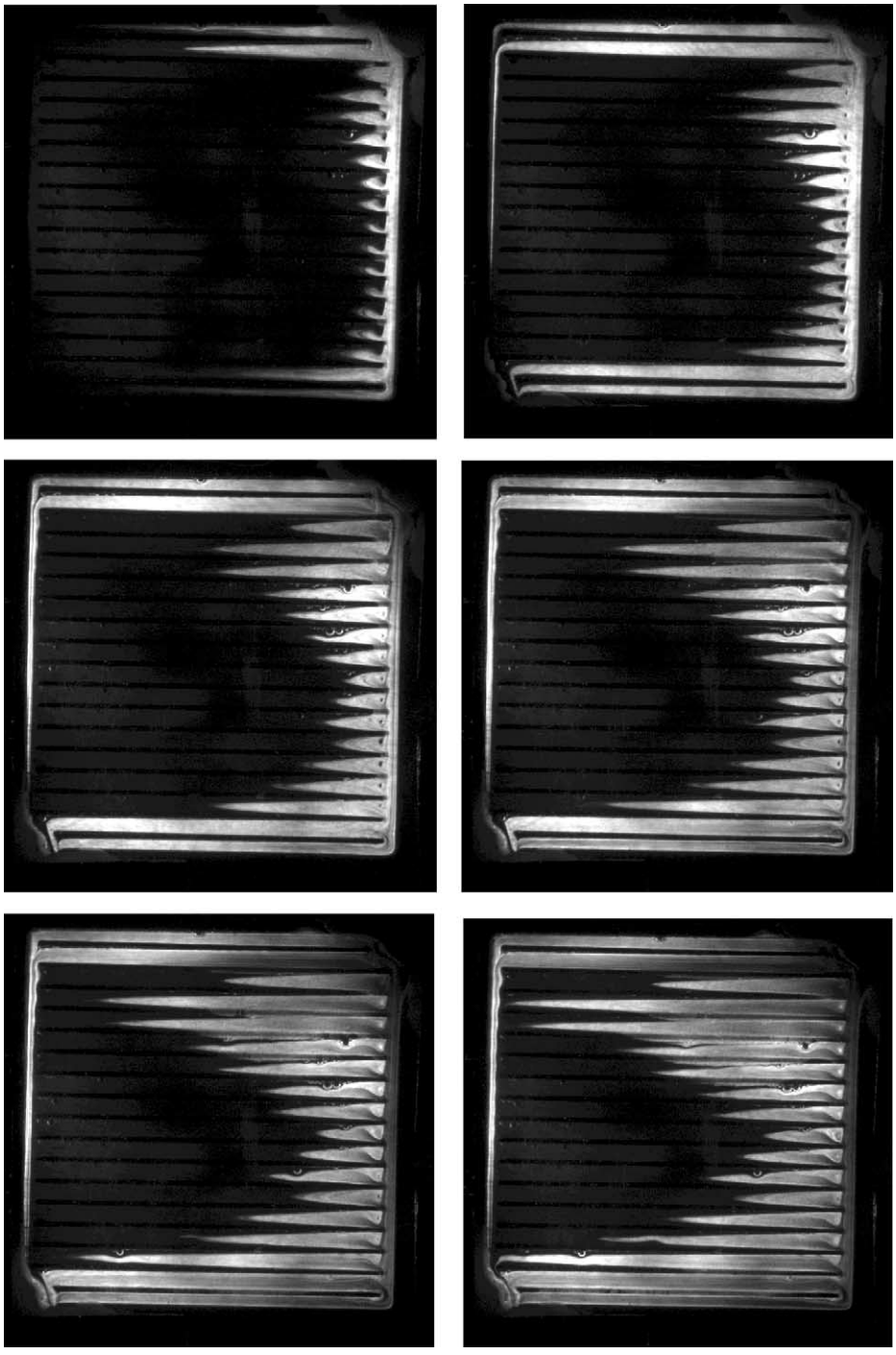

Fig. 9. Temporal sequence showing the advance of the dyed fluid. Images are separated by 0.5 s. Glycerin + water flow rate is 230 ml min^{-1}.

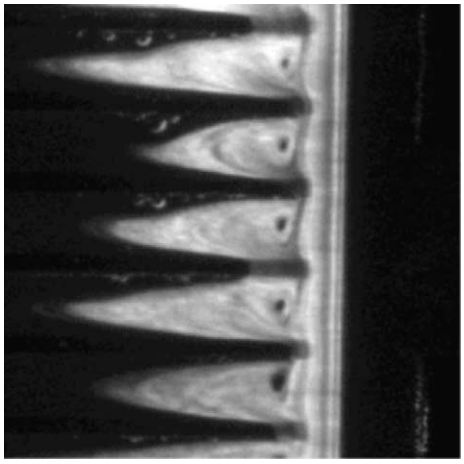

Fig. 10. Close up detail of the recirculation bubble at the entrance of the central channels.

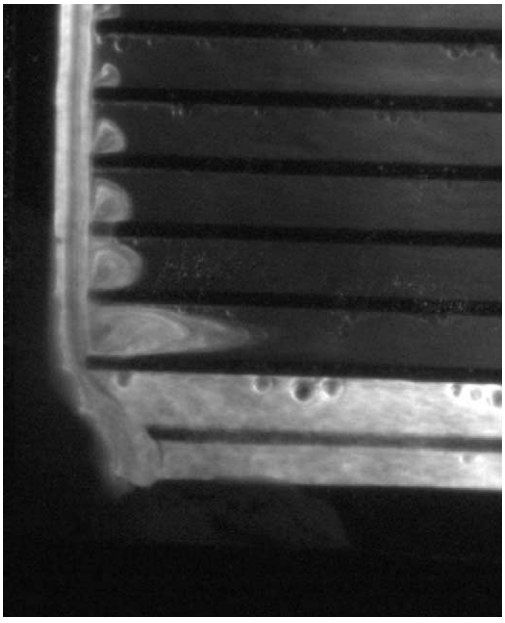

Fig. 11. Close up detail of the plate outlet.

to be outlined. It is clearly observed that a recirculation bubble forms in the entrance of each channel, in particular in the central zone of the plate (Fig. 10). This feature substantially decreases the free inlet area for these channels, and contributes to explain the reduced liquid entrance in them. The lower velocity in the third channel, compared to the one immediately below it is partly due to the angle that the injection port forms with the plate. As a matter of fact, the flow along the central channels is so slow that in certain cases it is possible to observe liquid entering through the exit (Fig. 11).

Numerical simulation also shows similar results, and with a good agreement with the experiments. Following the thorough discussion in the Section 5, the intermediate mesh (138×138) has enough precision to obtain reliable results in the numerical study. For this reason, all the results presented here are referred to this mesh, unless otherwise is pointed out. In Fig. 12, comparisons with the experiments are shown for a level of convergence β of order 10^{-20} for $E_{50,000-20,000}$, which seems very accurate, taken into account that a 2D approximation has being used. In order to ease the comparison, for the numerical simulation a flow rate of $230\,\mathrm{ml\,min^{-1}}$ of glycerin–water mixture has been considered, which corresponds to one of those used in the experiments. The agreement with the experimental data is quite noticeable and certainly corroborates the poor performance of the design for the bipolar plate studied in the present work. Again, it has been verified that the flow circulates with a higher velocity through the upper, lower and lateral channels. Their corresponding pressure and velocity maps are shown in Figs. 13 and 14, respectively. Numbers at the two sides of Fig. 13 correspond to the pressure values at the entrance and exit of each channel, respectively. It may be seen that the pressure drop is significantly higher at the channels that carry more fluid. As the density is conserved, this drive is expressed in higher velocities through those channels, as shown in Fig. 14. Both figures show a physical meaningful fluid field.

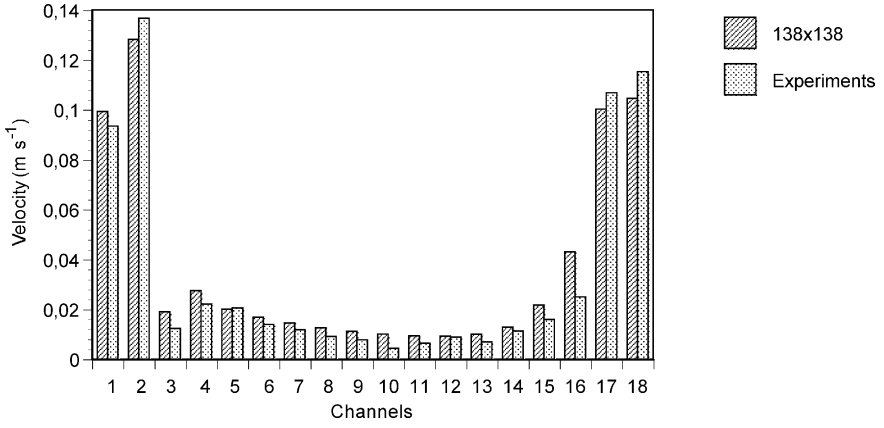

Fig. 12. Average velocities values calculated from the experiments, compared with those obtained by numerical simulation using the 138×138 grid and 50,000 iteration steps.

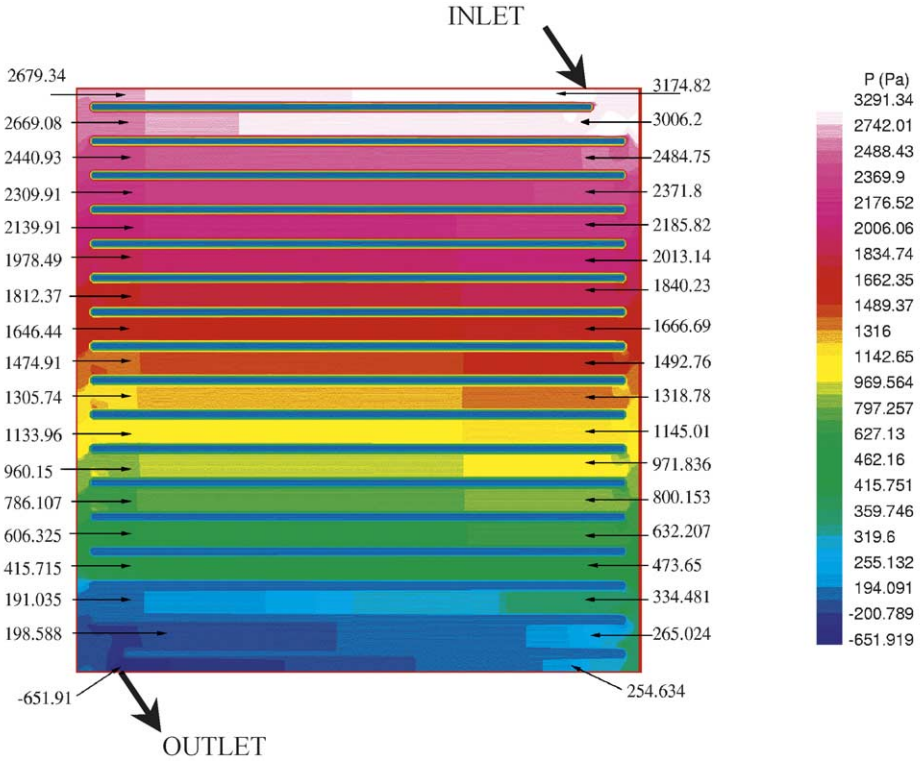

Fig. 13. Pressure map obtained from the numerical simulation with the same experimental conditions as in Fig. 12.

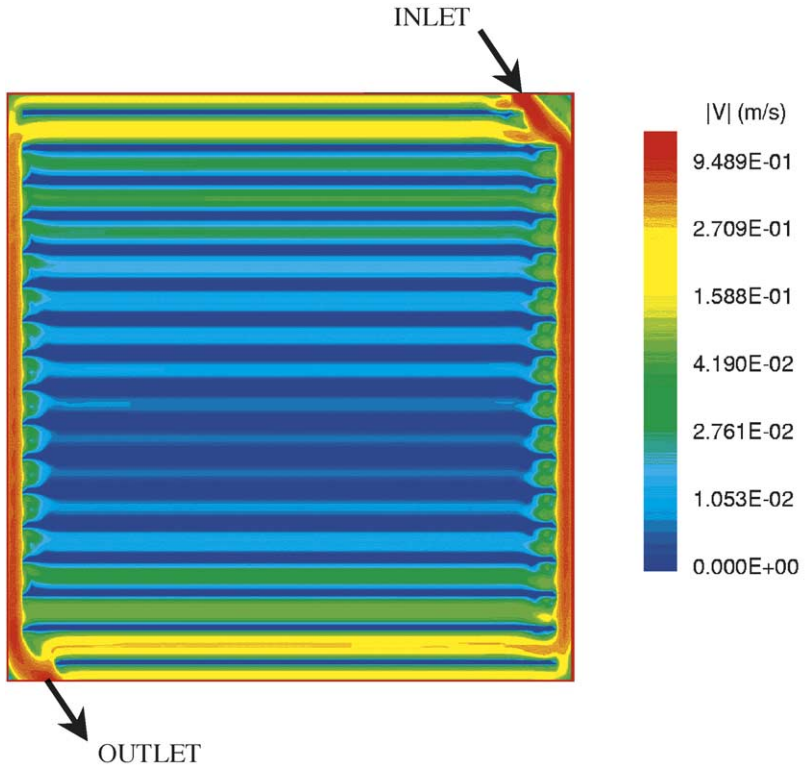

Fig. 14. The corresponding velocity map obtained from the numerical simulation for the conditions in Fig. 12.

Fig. 15 shows a zoom of the region near the entrance, showing velocity (left) and pressure fields with streamlines (right). Streamlines are used to feature the position of the eddy, which, as mentioned above, has a large influence on the distribution of the flow in the bipolar plate. The background depicts the pressure isocontour levels and velocity modulus, respectively. As it has been discussed in the experimental results, it can also be observed the existence of recirculation bubbles at the entrance of the horizontal channels. Although most of the fluid tends to flow down through the lateral channel, a significant amount of fluid is driven through the first two channels. The ultimate reason is probably the higher pressures originated near the zones where the fluid impinges against the bottom rib of the second channel. These higher-pressure areas near the entrance of the channels force the fluid to flow preferably through those channels. Fig. 16 shows the pressure and velocity field, as in Fig. 12, for the first channels but at the zone opposite to the entrance.

Figs. 17 and 18 show the behavior of the velocity and pressure at the bottom of the bipolar plate. It is important to note the increase in the pressure drop of the two last channels, which can also be verified analyzing the numerical values depicted in Fig. 13. This fact motivates that a large amount of fluid flows through channels 17 and 18 causing an increase of the velocity in this part of the plate. At the same time, it should also be noted that there is no recirculation bubble (or it is very weak) in the entrance of these channels. It is evident that this complex flow behavior is both studied and explained in an easy way using numerical simulation analysis. A slight shifting of the conditions in this area may cause an increase

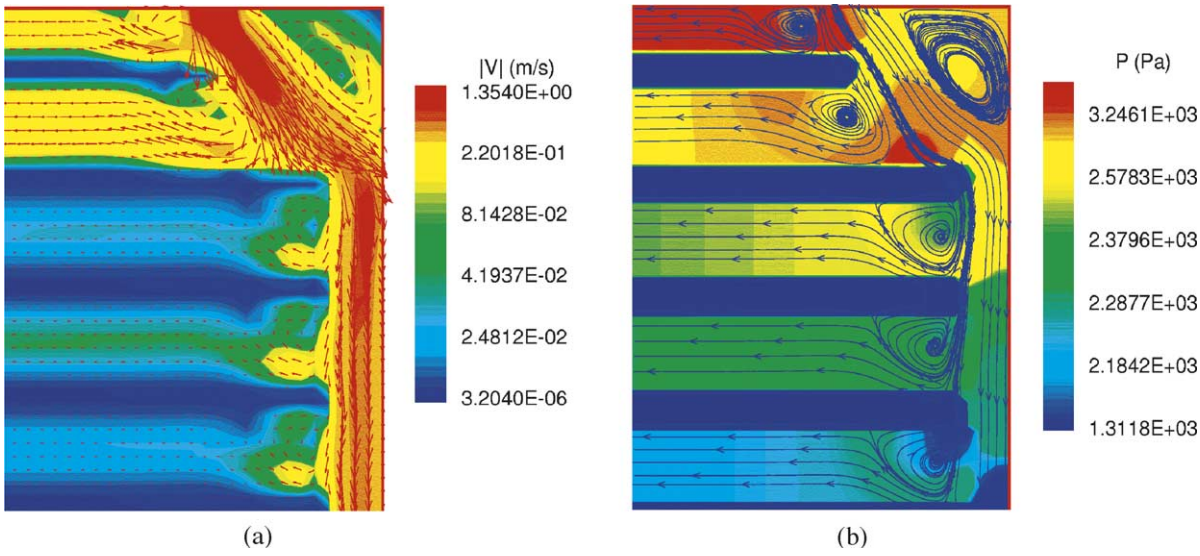

Fig. 15. Zoom of the region near the entrance of the flow at the bipolar plate showing the velocity (a) and pressure fields (b). Streamlines depict the position of the eddies.

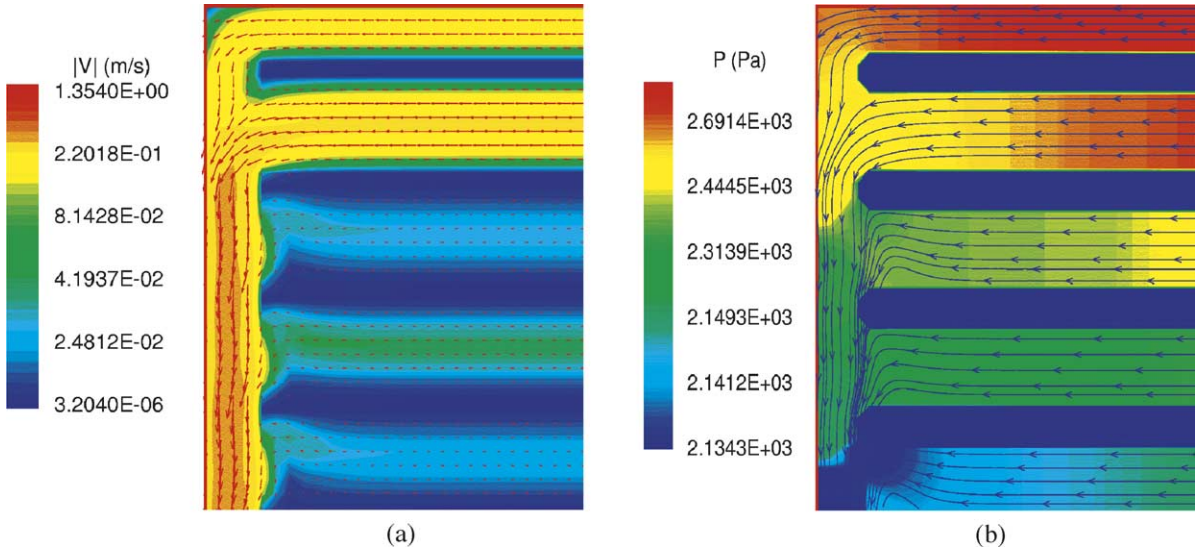

Fig. 16. Velocity (a) and pressure (b) fields for the first channels to the zone corresponding to the discharge of flow to the left lateral channel.

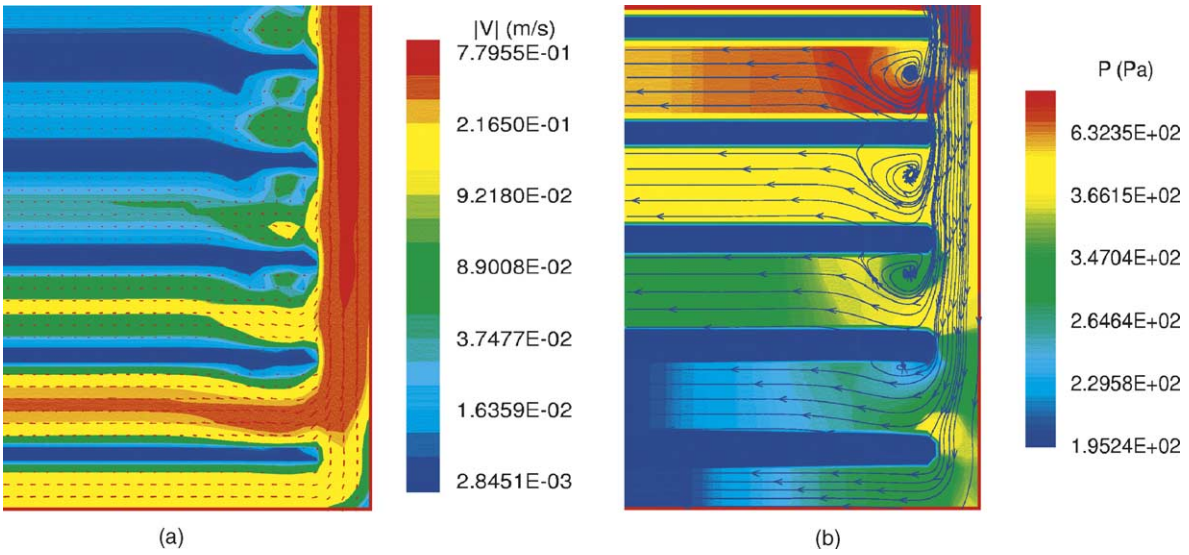

Fig. 17. Zoom image showing the velocity (a) and pressure (b) fields for the bottom channels to the zone corresponding to the entrance of flow.

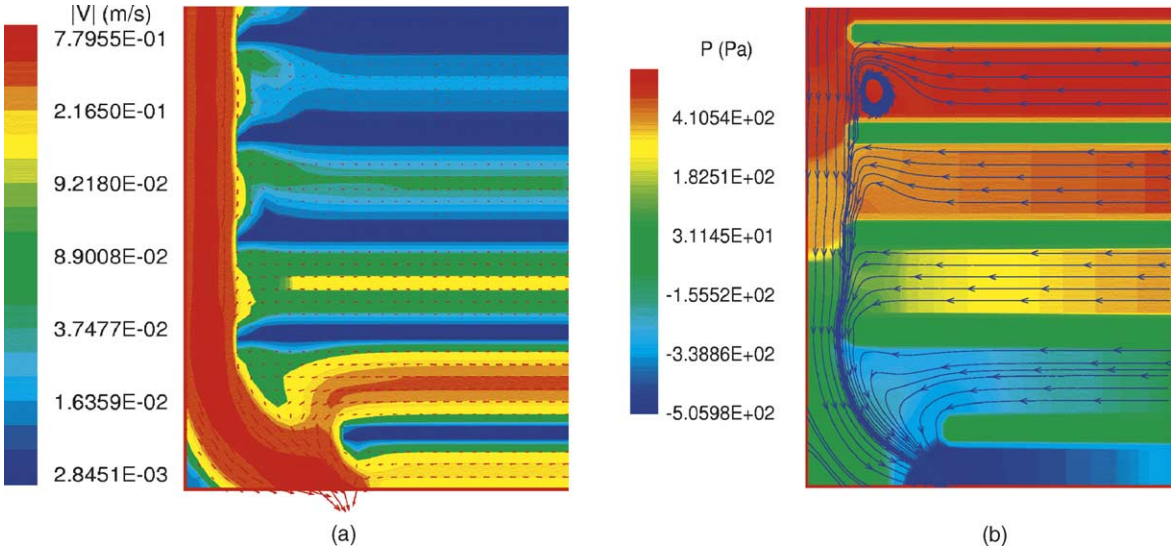

Fig. 18. Zoom of the region close to the exit of the flow to the bipolar plate showing the velocity (a) and pressure fields (b).

of the amount of flow through this channel and, as mentioned in the Section 5, may be the cause for the slower convergence of the velocity in that channel.

It should be pointed out that the deficient two-dimensional flow distribution observed in both experiments and numerical simulations is only representative of the particular bipolar plate topology tested in this work. Even when similar non-homogeneous flow patterns have been previously verified, for example, for the square spot gas flow topology [11,12], the present results cannot be extrapolated to other plate geometries. It is also known that with serpentine and interdigitated designs, as well as with flat porous plates; the gas flow can be more uniformly distributed over the whole electrode area. However, a drawback when these bipolar plates are used is that higher pressures are required for the gas to reach the electrodes, and some designs are difficult to manufacture. These disadvantages are overcome by the series–parallel distribution scheme, where a preferred flow path is maintained but with reduced pressure drops. Studies similar to the one here presented could be performed with alternative plate models, assessing and comparing the efficiency of the gas flow distribution in the cell plane.

7. Conclusions

Based on flow visualization and velocity measurement results, a worrying difference in the velocity values inside a parallel channel bipolar plate has been found. At the same time, the similitude between the dye patterns obtained circu-

lating water and a glycerin–water mixture for the two flow conditions tested demonstrates a weak dependence on both flow velocity and physical properties of the fluids. It is evident that the bipolar plate tested does not satisfy the requirements of homogeneous distribution of the flow over the electrodes. The presence of channels along which the fluid circulates very slowly, compared to the preferred paths through the lateral channels will probably lead to an unbalanced use of the catalyst, and an overall efficiency lower than expected. This non-homogeneity can be partly explained by the formation of recirculation bubbles at the channel entrance in the central zone of the plate. This effect could be alleviated by modifying the channel entrance, avoiding the connection at right angle with the channels. Simulations performed with a finite volume code have shown an excellent agreement with the measurements. In the future, this tool could be advantageously used to validate design modifications.

At least in the tested conditions, it seems evident that the design of this particular bipolar plate could be substantially improved, optimizing the distribution of the reactant gases inside the fuel cell.

Acknowledgement

This research has been partially supported by the Network of Fuel Cell Batteries of the Spanish Council for Scientific Research.

References

[1] Hydrogen, Energy and Fuel Cells—A vision for our future, High Level Group for Hydrogen and Fuel Cells, Summary Report, June 2003.
[2] V. Gurau, H. Liu, S. Kakaç, Two-dimensional model for proton exchange membrane fuel cells, AIChE J. 44 (11) (1998) 2410–2422.
[3] P. Costamagna, Transport phenomena in polymeric membrane fuel cells, Chem. Eng. Sci. 56 (2001) 323–332.
[4] L. Wang, A. Husar, T. Zhou, H. Liu, A parametric study of PEMFC performance, Int. J. Hydrogen Energy 28 (2003) 1263–1272.
[5] A.B. Geiger, A. Tsukada, E. Lehmann, P. Vontobel, G.G. Scherer, In situ investigation of two-phase flow patterns in flow fields of PEFC's using neutron radiography, Fuel Cells 2 (2) (2002) 92–98.
[6] G. Bender, M.S. Wilson, T.A. Zawodzinski, Further refinements in the segmented cell approach to diagnosing performance in polymer electrolyte fuel cells, J. Power Sources 123 (2) (2003) 163–171.
[7] K. Tüber, D. Pócza, Ch. Hebling, Visualization of water buildup in the cathode of a transparent PEM fuel cell, J. Power Sources 124 (2) (2003) 403–414.
[8] M.M. Mench, Q.L. Dong, C.Y. Wang, In situ water distribution measurements in a polymer electrolyte fuel cell, J. Power Sources 124 (1) (2003) 90–98.
[9] T. Bewer, T. Beckman, H. Dohle, J. Mergel, D. Stolten, Novel method for investigation of two-phase flow in liquid feed direct methanol fuel cells using an aqueous H_2O_2 solution, J. Power Sources 125 (1) (2004) 1–9.
[10] V. Mehta, J.S. Cooper, Review and analysis of PEM fuel cell design and manufacturing, J Power Sources 114 (2003) 32–53.
[11] L. Carrette, K.A. Friedrich, U. Stimming, Fuel Cells–fundamentals and applications, Fuel Cells 1 (1) (2001) 5–39.
[12] P. Costamagna, S. Srinivasan, Quantum jumps in the PEMFC science and technology from the 1960s to the year. Part II. Engineering, technology development and application aspects, J. Power Sources 102 (2001) 253–269.
[13] E. Hontañón, M.J. Escudero, C. Bautista, P. García-Ybarra, L. Daza, Optimization of flow-field in polymer electrolyte membrane fuel cells using computational fluid dynamics techniques, J. Power Sources 86 (1–2) (2000) 363–368.
[14] H. Dohle, R. Jung, N. Kimiaie, J. Mergel, M. Müller, Interaction between the difussion layer and the flow field of polymer electrolite fue cells – experiments and numerical simulations, J. Power Sources 124 (2) (2003) 371–384.
[15] Personal communication with researchers of the National Institute of Aerospatial Technique (I.N.T.A.) of Spain.
[16] R.H. Perry, D.W. Green, J.O. Maloney, Perry's Chemical Engineers Handbook, Sixth ed., McGraw-Hill, 1984.
[17] F.M. White, Fluid Mechanics, McGraw Hill, USA, 1979.
[18] U. Brackmann, Lambdachrome Laser Dyes, Lambda Physik GmbH, Göttingen, Germany, 1994, pp. 160–161.
[19] J.H. Ferziger, M. Peric, Computational Methods for Fluid Dynamics. Springer-Verlag, 2002.
[20] S.V. Patankar, Numerical Heat Transfer and Fluid Flow, McGraw-Hill, New York, USA, 1980.